How to cite: *Angew. Chem. Int. Ed.* **2021**, *60*, 26210–26217
International Edition: doi.org/10.1002/anie.202111265
German Edition: doi.org/10.1002/ange.202111265

CO_2 Reduction

Predesign of Catalytically Active Sites via Stable Coordination Cluster Model System for Electroreduction of CO_2 to Ethylene

Yun-Feng Lu[+], Long-Zhang Dong[+], Jiang Liu, Ru-Xin Yang, Jing-Jing Liu, Yu Zhang, Lei Zhang, Yi-Rong Wang, Shun-Li Li, and Ya-Qian Lan**

Abstract: *Purposefully designing the well-defined catalysts for the selective electroreduction of CO_2 to C_2H_4 is an extremely important but challenging work. In this work, three crystalline trinuclear copper clusters (**Cu_3-X**, $X = Cl^-$, Br^-, NO_3^-) have been designed, containing three active Cu sites with the identical coordination environment and appropriate spatial distance, delivering high selectivity for the electrocatalytic reduction of CO_2 to C_2H_4. The highest faradaic efficiency of **Cu_3-X** for CO_2-to-C_2H_4 conversion can be adjusted from 31.90% to 55.01% by simply replacing the counter anions (NO_3^-, Cl^-, Br^-). The DFT calculation results verify that **Cu_3-X** can facilitate the C–C coupling of identical *CHO intermediates, subsequently forming molecular symmetrical C_2H_4 product. This work provides an important molecular model system and a new design perspective for electroreduction of CO_2 to C_2 products with symmetrical molecular structure.*

Introduction

Electroreduction of CO_2 to highly valued carbon-based reduction product is recognized as one of the most promising and significant technologies to achieve global carbon neutrality.[1] As a basic chemical raw material with high volumetric energy density, the output of C_2H_4 is one of the crucial indicators to measure the development level of a country's petrochemical industry.[2] Therefore, it has been a quite important but challenging goal in the field of electrochemical CO_2 reduction reaction (CO_2RR) to construct the well-defined electrocatalysts for the conversion of CO_2 to C_2H_4 with high selectivity and efficiency.[3] In recent years, copper-based materials have been widely accepted as efficient catalysts for electrocatalytic reduction of CO_2 to C_2H_4.[4] Furthermore, a large number of tailoring strategies, including crystalline faceting,[5] multimetallic alloying,[6] multicomponent doping[7] and morphology controlling,[8] etc., have been applied to Cu-based catalysts to improve their activity and selectivity for electrochemical conversion of CO_2 to C_2H_4. Although significant progress has been made in the electrocatalytic reduction of CO_2 to C_2H_4, it is still very difficult to design and synthesize catalysts with higher selectivity rationally due to the complicated reaction process and the indistinct reaction mechanism. To solve this problem, it is quite necessary to design a catalyst model with atomically accurately structural information and further reveal the catalytic mechanism of CO_2 to the specific C_2H_4 product.

Considering the symmetrical molecular structure of C_2H_4, we speculate that the constructed catalysts for efficient electrocatalytic reduction of CO_2 to C_2H_4 may need to be endowed with the following characteristics at the same time: (i) at least two catalytically active sites to adsorb two or more CO_2 molecules simultaneously; (ii) adjacent catalytically active sites with the same coordination environment to allow the adsorbed CO_2 molecules to be activated in nearly the same direction and speed; (iii) suitable spatial distances between active sites to achieve the C–C coupling between the identical reaction intermediates. To sum up, the design and synthesis of precise structural model catalysts with the above-mentioned three characteristics can help to reveal the reaction mechanism of electrocatalytic conversion of CO_2 to C_2H_4. Metal-organic coordination complexes with accurate crystal structural information can be reasonably designed and functionalized according to specific requirements and the unique characteristics bring the materials obvious advantages in the construction of model catalysts.[9] However, the materials have not been widely used as electrocatalysts at present, owing to the difficulty of maintaining the structural stability for most metal-organic coordination complexes in the harsh alkaline electrolyte of the electrochemical test. According to the hard and soft acids and bases (HSAB) theory, the chemical stability of the compounds could be greatly enhanced by assembling Cu^{2+} and appropriate basic N-donor ligands, which has inspired us deeply.[10] The accurate structure-property relationship can be established by using the well-defined crystalline model catalysts with the improved chemical stability in electrocatalytic CO_2RR. The tactic is of great significance for broadening the application of crystalline materials as well as investigating the mechanism of electrocatalytic CO_2RR.

[*] Y.-F. Lu,[+] L.-Z. Dong,[+] Dr. J. Liu, R.-X. Yang, Dr. Y. Zhang, Y.-R. Wang, Prof. S.-L. Li, Prof. Y.-Q. Lan
Jiangsu Collaborative Innovation Centre of Biomedical Functional Materials, Jiangsu Key Laboratory of New Power Batteries, School of Chemistry and Materials Science, Nanjing Normal University
Nanjing 210023 (P. R. China)
E-mail: liuj@njnu.edu.cn
yqlan@njnu.edu.cn
Homepage: http://www.yqlangroup.com
Dr. J. Liu, J.-J. Liu, Dr. L. Zhang, Prof. Y.-Q. Lan
School of Chemistry, South China Normal University
Guangzhou 510006 (P. R. China)
E-mail: yqlan@m.scnu.edu.cn
[+] These authors contributed equally to this work.
Supporting information and the ORCID identification number(s) for the author(s) of this article can be found under: https://doi.org/10.1002/anie.202111265.

Taking the above considerations into account, three isomorphic **Cu_3-X** clusters (**Cu_3-Cl**, **Cu_3-Br**, **Cu_3-NO_3**) have been designed and synthesized, which are composed of the oxygen centered trinuclear copper cluster ($\{Cu_3(\mu_3\text{-}OH)(\mu\text{-}pz)_3(Im)_3\}^{2+}$) (denoted as $\{Cu_3\}$) and counter anions. Due to the high symmetry along the crystallographic C_3 axis, the adjacent catalytically active Cu sites in **Cu_3-X** clusters own the identical coordination environment, which is likely to be beneficial for the parallel attack and simultaneous activation of multiple CO_2 molecules. In addition, the appropriate distances (3.268, 3.266 and 3.364 Å for **Cu_3-Cl**, **Cu_3-Br** and **Cu_3-NO_3**, respectively) between the adjacent active sites may facilitate the C–C coupling of carbon-based reaction intermediates. It can be seen that the structural features of **Cu_3-X** meet the aforementioned speculation of the model catalysts for the electroreduction of CO_2 to C_2H_4 fundamentally. Moreover, it is worth noting that these three clusters possess superior electrochemical stability and can be used as persistent heterogeneous catalysts in the process of electrocatalytic CO_2RR. When the **Cu_3-X** are applied to CO_2RR, all the three clusters succeed in realizing the electrochemical reduction of CO_2 to C_2H_4. The experimental results demonstrate the validity of the initial idea in designing crystalline model catalysts for electrocatalytic CO_2-to-C_2H_4 conversion to some extent. The CO_2-to-C_2H_4 conversion selectivity of **Cu_3-X** clusters is obviously different with the change of counter anions in their crystal structures. The **Cu_3-Br** exhibits a superior faradaic efficiency (FE) of 55.01% for C_2H_4 generation with a large current density (129.58 mA cm^{-2}) at −0.7 V (vs. reversible hydrogen electrode, RHE) and can basically maintain the selectivity in a wide potential range (−0.7 V to −1.1 V). While the FEs of C_2H_4 catalyzed by **Cu_3-Cl** and **Cu_3-NO_3** reach to the peak value of 47.68% and 31.90% at −0.9 V and −0.8 V, respectively. Notably, the catalytic performance of **Cu_3-Br** is one of the most excellent stable metal-organic complex catalysts for electrochemical CO_2-to-C_2H_4 conversion to date. The different catalytic performance of the three clusters originates from the counter anions, which own unequal volume and bind with the ($\{Cu_3(\mu_3\text{-}OH)(\mu\text{-}pz)_3(Im)_3\}^{2+}$) unit in different strength as well, thus affecting the number of CO_2 molecules attacking the catalytically active sites at the same time and the optimal catalytic selectivity of the three catalysts for C_2H_4. The theoretical calculation results further confirm the prediction: the two adjacent catalytically active centers in **Cu_3-X** with the same coordination environment are in favor of the C–C coupling of active intermediate CH*O adsorbed on them and thus promote the high selective electroconversion of CO_2 to symmetrical C_2H_4 molecule.

Results and Discussion

Single-crystal X-ray diffraction analysis (SCXRD) reveals that **Cu_3-X** crystallize in the same rhombohedral space group *R*3m (Table S1) and their stacking patterns are almost identical (Figure S1). The asymmetric units of **Cu_3-X** clusters contain an independent Cu^{2+} ion, 1/3 μ_3-OH, 1/2 pyrazole (pz), one imidazole (Im) molecule and two 1/3 **X** ions (**X** = counter anions, Figure S2). As shown in Figure 1 a–d, **Cu_3-X**

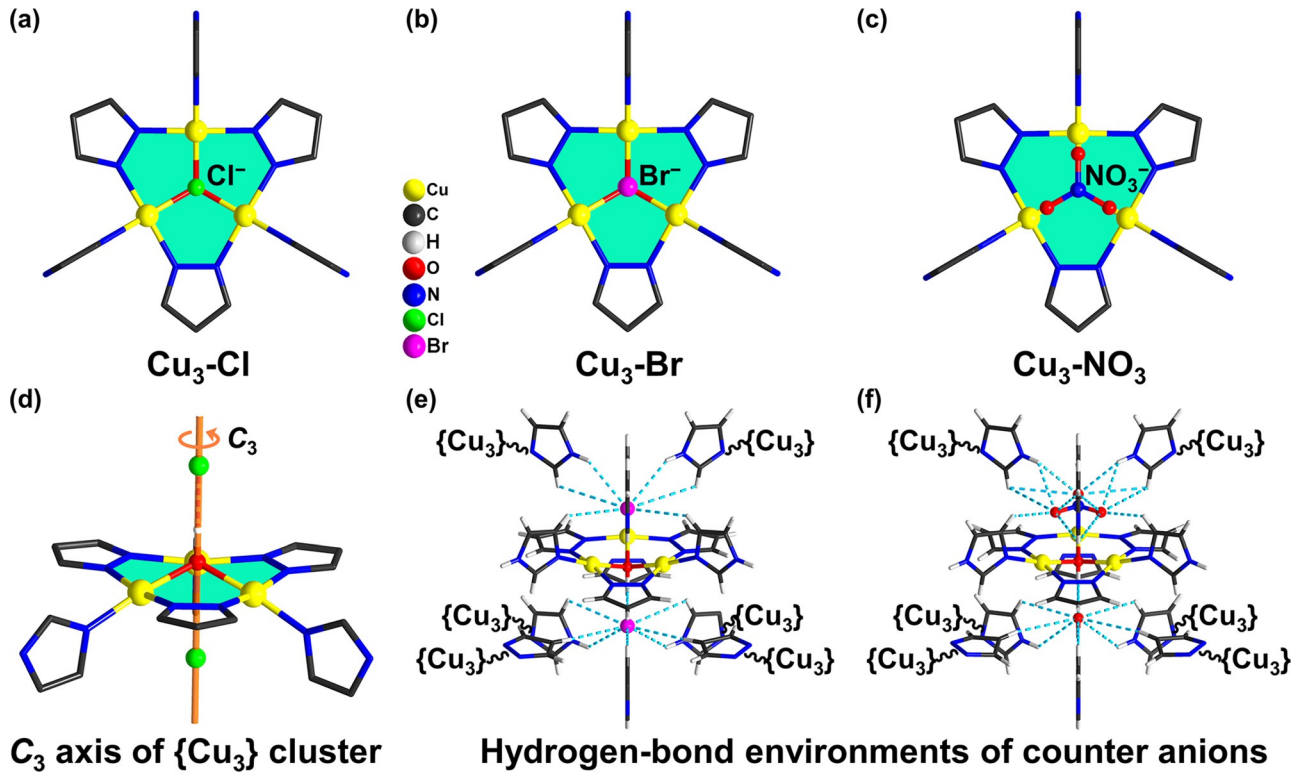

Figure 1. The molecularly structure characteristics of **Cu_3-X.** The plane defined by the three Cu^{2+} ions in (a) **Cu_3-Cl**, (b) **Cu_3-Br** and (c) **Cu_3-NO_3**. (d) The C_3 axis in **Cu_3-X** clusters. (e,f) The hydrogen-bond environments of counter anions in **Cu_3-Br** and **Cu_3-NO_3**, respectively.

contain the same $Cu_3(\mu_3\text{-OH})$ core supported by equatorial bridging pyrazole ligands to form trinuclear triangular $\{Cu_3(\mu_3\text{-OH})(\mu\text{-pz})_3\}^{2+}$ unit, while the imidazole accomplishes the square-planar coordination of the Cu^{2+} ion. It should be noted that the Cu^{2+} ions of **Cu_3-X** bind no other ligands in the axial direction, the coordination-unsaturated metal sites will exhibit excellent catalytic activity by providing enough space for small molecular substrates to attack. Furthermore, the axial positions of all the Cu^{2+} ions in the three clusters are parallel, which is conducive to bind the substrates to the catalytic sites in the same coordination mode and direction. The values of the selected bond distances and bond angles in the crystal structure are shown in Table S2. The main difference among the three clusters is the diversity of counter anions in their structures: there are two Cl^- ions in **Cu_3-Cl**, two Br^- ions in **Cu_3-Br**, while a NO_3^- and a OH^- in **Cu_3-NO_3** acting as counter anions, respectively. Interestingly, the counter anions situate symmetrically above and below the plane defined by the three Cu^{2+} ions and there is a crystallographic C_3 axis running through the center of the counter anions and the μ_3-OH (Figure 1 d). The counter anions in **Cu_3-X** form a large number of hydrogen bonds with the adjacent hydrogen atoms of μ_3-OH group, pyrazole and imidazole molecules (Figure 1 e,f, Figure S3–S4 and Table S3–S5). It can be clearly seen that there are more hydrogen bonds in **Cu_3-NO_3** than **Cu_3-Cl** and **Cu_3-Br**. Due to the formation of numerous hydrogen bonds, the counter anions will not be dissociated easily. It is worth noting that the volume of NO_3^- is much larger than that of Cl^- and Br^- so that it could almost completely block a half coordination space of Cu^{2+} ions in the structure, which may make it difficult for the substrates to attack directly. Therefore, we speculate that the catalytic performance of **Cu_3-NO_3** may not be as good as that of **Cu_3-Cl** and **Cu_3-Br**.

The Powder X-ray diffraction (PXRD) patterns of **Cu_3-Cl** (spindle crystals), **Cu_3-Br** (parallelepiped crystals) and **Cu_3-NO_3** (rhombic dodecahedron crystals) and the simulated patterns derived from single crystal X-rays are well-matched, which confirms that the as-synthesized samples owing excellent crystallinity and high purity (Figure S5–S6). The chemical stability is evaluated by immersing 20 mg sample into 10 mL 0.5 M KOH aqueous solution for 24 h. The PXRD patterns of the samples after immersion show no difference from those of the as-synthesized samples, implying that the **Cu_3-X** could maintain the structural integrity in alkaline solution (Figure S6). At the same time, the thermogravimetric analysis (TGA) is carried out under oxygen atmosphere to evaluate the thermal stability of the **Cu_3-X** (Figure S8) and the results illustrate that all the three samples possess good thermal stabilities over 240 °C. The CO_2 adsorption isotherms of the **Cu_3-X** are tested at 273 K and 1 atm to explore the adsorption capacity of the samples for CO_2. As shown in Figure S9, the CO_2 uptakes can be estimated to be 11.5025, 12.4426 and 10.7147 $cm^3 g^{-1}$, respectively. In summary, the structural characteristics and high chemical stability of **Cu_3-X** clusters endow them with potential as catalysts for electrocatalytic CO_2-to-C_2H_4 conversion.

According to the stability test results of the as-synthesized samples, 0.5 M KOH aqueous solution is selected as the electrolyte for electrocatalytic CO_2RR test in the flow cell. At

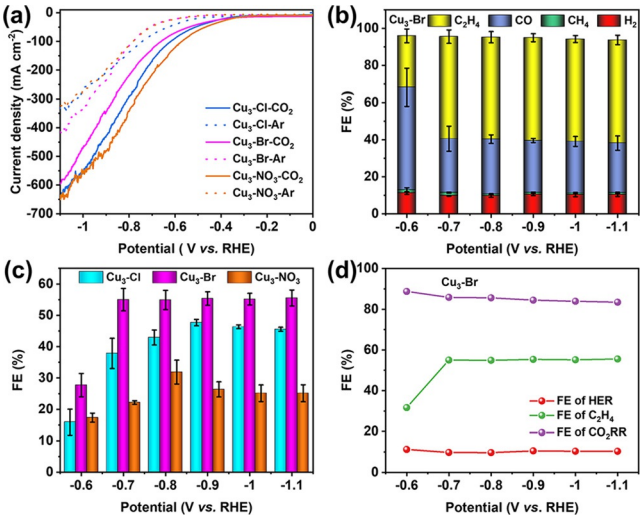

Figure 2. The activity and selectivity of **Cu_3-X** for CO_2RR. (a) Linear sweep voltammetry (LSV) curves of **Cu_3-Cl**, **Cu_3-Br** and **Cu_3-NO_3** in Ar and CO_2 atmosphere. (b) Faradaic efficiency (FE) (H_2, CH_4, CO and C_2H_4) of **Cu_3-Br** at different potentials (−0.6 V to −1.1 V). (c) The contrast of $FE_{C_2H_4}$ for CO_2RR catalyzed by **Cu_3-Cl**, **Cu_3-Br** and **Cu_3-NO_3** at different applied potentials (−0.6 V to −1.1 V). (d) The FEs for HER, total CO_2RR and C_2H_4 conversion catalyzed by **Cu_3-Br**.

first, the linear cyclic voltammetry (LSV) curves are measured in the atmosphere of CO_2 and Ar separately (Figure 2 a and Figure S10) to preliminary characterize the CO_2RR activity of the **Cu_3-X**. The LSV curves show that the onset potential of **Cu_3-X** in CO_2 stream is more positive than that in Ar, which testifies the possibility of the catalysts for CO_2RR. Moreover, the current density in CO_2 is much higher than that in Ar atmosphere, showing that the intrinsic activity of the catalysts is for CO_2RR rather than hydrogen evolution reaction (HER). The current densities of **Cu_3-Cl**, **Cu_3-Br** and **Cu_3-NO_3** can reach to 635.79, 595.74 and 650.49 mA cm^{-2} at −1.1 V, respectively, further testifying the possibly favorable activity for CO_2RR.

To evaluate the catalytic selectivity of the catalysts to the formation of different products, the CO_2 electroreduction experiments are performed at different potentials (−0.6 V to −1.1 V) and the gaseous reduction products are detected by gas chromatography (GC) and the liquid products are analyzed by nuclear magnetic resonance (NMR). As shown in Figure 2 b, Table S6 and Figure S11–S12, the gaseous reduction products of CO_2RR catalyzed by the **Cu_3-X** are mainly C_2H_4, CO, H_2 and CH_4. Additionally, trace liquid products have been detected by NMR (Figure S13). However, the concentration of liquid products in the electrolyte is lower than the detection limit, so that it cannot be accurately quantified. The blank carbon paper has been used as electrocatalyst to eliminate the influence of carbon paper on catalytic performance. The results in Figure S14 illustrate that the main product of the CO_2RR when catalyzed by carbon paper is H_2. The Figure 2 b and Figure S12 display that C_2H_4 and CO are the main competing products in the reduction products and furthermore, the FE_{H_2} and FE_{CH_4} remain almost unchanged at all test potentials. In detail, **Cu_3-Br** gives the highest FE_{CO} (55.3 %) at −0.6 V, along with

27.71 % $FE_{C_2H_4}$, 11.22 % FE_{H_2} and 0.18 % FE_{CH_4}. Subsequently, when the potential increases to −0.7 V, the $FE_{C_2H_4}$ reaches up to 55.01 % with a large current density (129.58 mA cm^{-2}) and the selectivity is nearly invariable in a wide potential range (−0.7 V to −1.1 V). As for **Cu_3-Cl**, it gives 70.89 % FE_{CO}, 15.92 % $FE_{C_2H_4}$, 7.68 % FE_{H_2} and 0.66 % FE_{CH_4} at −0.6 V. With the increase of potential, the faradaic efficiency of the main reduction product (C_2H_4), increases gradually and reaches maximum value of 47.68 % at −0.9 V, and then decreases. In contrast, **Cu_3-NO_3** gives 61.86 % FE_{CO}, 17.34 % $FE_{C_2H_4}$, 14.84 % FE_{H_2} and 2.79 % FE_{CH_4} at −0.6 V. The change trend of **Cu_3-NO_3** is similar to that of **Cu_3-Cl**, and the $FE_{C_2H_4}$ peak of **Cu_3-NO_3** is 31.90 % at −0.8 V (Figure S12). For a clearer contrast, the yield distribution of C_2H_4 at different potentials is shown in Figure 2c, it can be seen that the $FE_{C_2H_4}$ of **Cu_3-Br** at each potential is higher than that of **Cu_3-Cl** and **Cu_3-NO_3**, showing the best catalytic performance among the three samples. The Figure 2d and Figure S15 show that the lowest FE_{CO_2RR} is 73.88 % of **Cu_3-NO_3** at −0.9 V, and the highest FE_{CO_2RR} is 88.73 % of **Cu_3-Br** at −0.6 V among the three samples, which further proves that the catalysts support CO_2RR much more strongly than the competitive reaction (HER).

To further reveal the superior activity of **Cu_3-Cl**, **Cu_3-Br** and **Cu_3-NO_3**, the partial current densities of C_2H_4, CO, H_2 and CH_4 at different potentials are calculated. As shown in Figure 3a, the partial C_2H_4 current densities of **Cu_3-Cl**, **Cu_3-Br** and **Cu_3-NO_3** can reach 289.70, 330.90 and 163.46 mA cm^{-2} at −1.1 V, respectively, which shows that the activity for C_2H_4 of **Cu_3-Br** is much better than **Cu_3-Cl** and **Cu_3-NO_3**. Besides, the partial current densities of **Cu_3-NO_3** for CO and H_2 are much larger than that of **Cu_3-Cl** and **Cu_3-Br**, which could also indicate that the activity of **Cu_3-NO_3** for C_2H_4 is inferior to that of **Cu_3-Cl** and **Cu_3-Br** (Figure S16).

From the cyclic voltammetry (CV) curves (Figure S17), the values of electrochemical double-layer capacitance

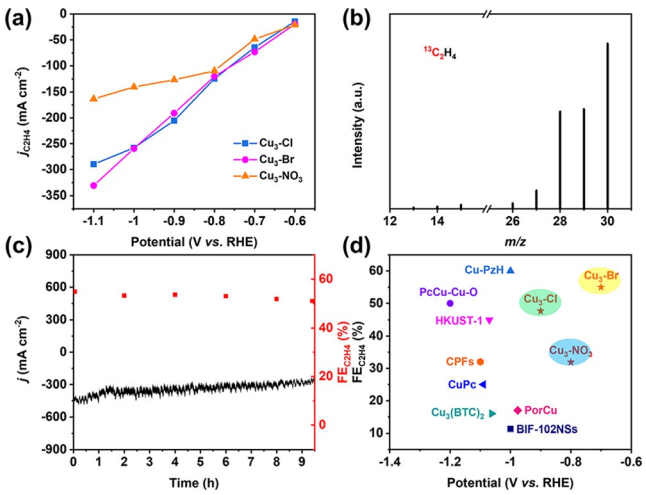

Figure 3. Characterization of **Cu_3-X**. (a) Partial current density of C_2H_4 of **Cu_3-X** at different applied potentials (−0.6 V to −1.1 V). (b) The mass spectra of $^{13}C_2H_4$ recorded under $^{13}CO_2$ atmosphere for **Cu_3-Br**. (c) Durability test of **Cu_3-Br** at the potential of −0.9 V vs. RHE. (d) The comparison of catalytic performance among the reported stable metal-organic complex electrocatalysts.

(C_{dl})[11] are calculated to evaluate the electrochemical active surface area (ECSA) of **Cu_3-Cl**, **Cu_3-Br** and **Cu_3-NO_3**. As shown in Figure S18, the C_{dl} values of the three samples are similar (0.207, 0.304 and 0.187 mF cm^{-2}), revealing that the three samples have the similar number of catalytic sites interacting with the electrolyte, which is consistent with the number of copper ions in the clusters. Additionally, the electrochemical impedance spectroscopy (EIS) tests of **Cu_3-X** are conducted at −0.8 V to investigate the electrocatalytic kinetics on the electrode/electrolyte surface during electrochemical CO_2RR. As shown by the Nyquist plots (Figure S19 and Table S7), **Cu_3-Br** exhibits the smallest charge transfer resistance (3.219 Ω) among the three samples, which means its fastest charge transfer rate from the catalyst surface to the reactant in the process of CO_2RR and correspondingly enhanced electrocatalytic activity and selectivity.

The isotope labeling experiment is carried out by using $^{13}CO_2$ as the substrate under the identical experimental conditions as that of $^{12}CO_2$ to reveal the carbon source in the electrochemical reduction products. The products are analyzed by gas chromatography and mass spectrometry. As shown in Figure 3b and Figure S20, the peaks at $m/z = 17$, 29 and 30 are ascribed to $^{13}CH_4$, ^{13}CO and $^{13}C_2H_4$, respectively, indicating that the CH_4, C_2H_4 and CO are indeed converted from the CO_2 reduction.

The excellent activity and selectivity of electrocatalytic CO_2RR attract us to further explore the catalytic durability of the catalyst to evaluate its catalytic performance and practical application potential. The short-time durability curves are shown in Figure S21, reflecting that all the three catalysts can preserve a stable current from −0.6 V to −1.1 V. The long-term durability of **Cu_3-Br** at −0.9 V is tested by testing $FE_{C_2H_4}$ intermittently with GC every 2 hour. The chronoamperometric curve (Figure 3c) tells that the current density of **Cu_3-Br** can basically maintain over 300 mA cm^{-2} and the $FE_{C_2H_4}$ remains at about 50 % during the durability test of 9.5 hours. However, the electrocatalytic durability is somewhat limited by harsh electrolysis conditions and traditional carbon paper support.[2b] In contrast, the electroreduction of CO_2 has been achieved directly in gas phase by using the membrane electrode assembly (MEA) in previous work, which could improve the $FE_{C_2H_4}$ and long-term stability of the catalysts by alleviating the mass transfer constraints and the severe electrolysis conditions.[6d,12] Therefore, if the **Cu_3-X** can be used as the catalysts in the MEA electrochemical cell, the catalytic performance is likely to be enhanced.

A series of comparative characterizations are carried out on the samples uniformly ground and loaded on carbon paper to further demonstrate the superior stability of the three catalysts. As shown in Figure S22, there is no obvious macroscopic morphological change of the samples in the process of electrochemical test. The PXRD patterns of the carbon papers coated with the samples before and after the electrocatalytic CO_2RR are well-matched, illustrating that the **Cu_3-X** could maintain their structural integrity during the test (Figure S23). It is worth noting that there are no peaks of Cu^0, Cu_2O or CuO in the PXRD patterns of **Cu_3-X** samples, which shows that the Cu^{2+} ions in the **Cu_3-X** are not transformed into Cu^0, Cu_2O or CuO. This can also be

confirmed by the ex situ and in situ Raman spectra of the samples. As shown in Figure S24, the Raman characteristic peaks of Cu_2O or CuO reported in the literature (146, 217, 310, 417, 520, 636, 810 cm^{-1} for Cu_2O and 298, 345, 632 cm^{-1} for CuO)[13] do not appear on the ex situ Raman spectra of **Cu_3-X** samples. At the same time, the in situ Raman spectra of the best-performing **Cu_3-Br** before and during the electrocatalytic CO_2RR at different applied potentials have been performed to further testify the structural stability of the catalysts under operating conditions. There are no new peaks appearing on the in situ Raman spectra (Figure S25) of the catalysts at various applied potentials during the CO_2RR process and the positions of the intrinsic peaks of **Cu_3-Br** do not shift obviously. All the Raman spectra illustrate that the **Cu_3-X** catalysts are stable during the electrocatalytic CO_2RR. In addition, the electronic states of **Cu_3-X** are determined by the XPS spectra of the samples. The contrast of the XPS spectra of Cu 2p (Figure S26) manifests that the Cu^{II} oxidant state in the catalysts keeps unchanged before and after the CO_2RR, which further proves the superior electrochemical stability of **Cu_3-X**.

Although the $FE_{C_2H_4}$ of **Cu_3-X** are lower than that of the most superior CO_2RR electrocatalysts (e.g., nanomaterials) reported so far, the precise structure-property relationship built by this crystalline model system can provide more insights into reaction mechanism for electrochemical CO_2-to-C_2H_4 conversion and the future design of more efficient electrocatalysts. Moreover, it deserves to be mentioned that the electrocatalytic performance of **Cu_3-Br** is comparable to those of the best-performing stable metal-organic complex electrocatalysts reported so far (Figure 3d and Table S8).[3,14] Compared with the electrocatalysts reported by our group recently, the **Cu_3-Br** could give $FE_{C_2H_4}$ of 55.01% at a lower potential (−0.7 V) and keep the selectivity basically unchanged in a wide potential range (−0.7 V to −1.1 V).[3c] It is noteworthy that the main competitive product of C_2H_4 is CO rather than H_2 when the CO_2RR is catalyzed by **Cu_3-X**, particularly the FE_{H_2} can be controlled below 15%, which means an important progress in the selectivity control of CO_2RR in aqueous solution.

The blocking effect of different volume of the counter anions on the catalytically active sites is displayed clearly in Figure S27. As we can see, the order of the volume of counter anions is $NO_3^- > Br^- > Cl^-$, so that the NO_3^- may completely block the attacking space of CO_2 molecules to the active Cu sites on its side, while Cl^- has the least effect on the coordination ability between the Cu sites and CO_2 substrate. When the effect of the volume of counter anions is reflected on the electrocatalytic performance of **Cu_3-X**, the order of the selectivity for electrocatalytic conversion of CO_2 to C_2H_4 is expected to be **Cu_3-Cl** > **Cu_3-Br** > **Cu_3-NO_3**. However, all the above experimental results have proved that **Cu_3-Br** has the best electrocatalytic performance for the reduction of CO_2 to C_2H_4, which greatly arouse our interests in further exploring the reason for this difference. For **Cu_3-Cl** and **Cu_3-Br** (Figure S1–S4), it could be found that there are no structural differences between the two clusters apart from the various volume of the counter anions. Besides, as mentioned above, a large quantity of comparative characterization results show that all the three clusters can maintain their structural integrity during the test. Therefore, based on the experimental results and structural analysis, we speculate reasonably that the volume of counter anions does not play a decisive role in the electrocatalytic performance difference between **Cu_3-Cl** and **Cu_3-Br**. The assumption is further affirmed by the theoretical calculation results.

The density functional theory (DFT) calculations are carried out to further explore the C–C coupling mechanism of the electrochemical CO_2-to-C_2H_4 conversion catalyzed by **Cu_3-X** clusters. The initial structures for calculation are simplified from the crystal structure of **Cu_3-X**, as shown in Figure S28. At first, the possible paths for C–C coupling have been explored. We have tried to speculate different possible paths of CO_2-to-C_2H_4 conversion above or below the plane formed by three Cu^{2+} ions. For the convenience of description, the side of μ_3-OH protruding from the plane is recorded as the downside while the other side is called the upside in the following paper. The steric hindrance caused by the protruding -OH is predominant on the downside, which seems unfavorable for intermediates coupling. Besides, the angle between the Cu sites on the downside is not conducive to the intermediate coupling, either. As a result, the upsides of **Cu_3-X** are selected as the main adsorption direction of the reactants.

Generally, the C–C coupling begins from *CO (* indicates the adsorption site) and the subsequent reaction will go through one of the four pathways (**SI** Computational Details).[15] In this study, the COCO and COCHO pathways are eliminated at first, because neither *CO*CO nor *CO*CHO could be optimized on the surfaces of **Cu_3-X**, which indicates that these intermediates adsorbed on the active Cu sites are not stable. In addition, the COHCOH coupling pathway cannot be optimized on **Cu_3-NO_3**, suggesting the exact C–C coupling pathway on **Cu_3-NO_3** is the CHOCHO pathway. The free energy diagrams (FEDs) for CHOCHO and COHCOH pathways are compared for all the upsides of **Cu_3-X** (Figure 4a–c and Figure S29). There is a clear show that the COHCOH coupling pathway possess a much higher ΔG_{0max} (ΔG_{0max} refers to the standard Gibbs energy, >1.5 eV) than that of the CHOCHO coupling pathway (<0.06 eV). Therefore, the C–C coupling of CO_2RR when catalyzed by **Cu_3-X** prefers to follow the CHOCHO pathway. Moreover, the dimerization energies on both sides of **Cu_3-X** are also compared in Figure 4a–c and Figure S30, which further illustrates that C–C coupling tends to take place on the upsides of the clusters.

As shown in Figure 4a–c, the calculation results show that the most active structure for C–C coupling is the **Cu_3-Br** that possesses the smallest ΔG_{0max} of −0.20 eV for the most endothermic elementary step. Following which are the **Cu_3-Cl** ($\Delta G_{0max} = -0.08$ eV) and the **Cu_3-NO_3** ($\Delta G_{0max} = 0.06$ eV). Therefore, the **Cu_3-Br** exhibits the best catalytic selectivity for the electrochemical CO_2-to-C_2H_4 conversion and the **Cu_3-NO_3** gives the lowest faradaic efficiency for C_2H_4 in theory, which is consistent with the experimental results of the electrochemical tests. According to the aforementioned results, it is speculated reasonably that the dipole (upward) direction of CHOCHO is the same as the direction of the

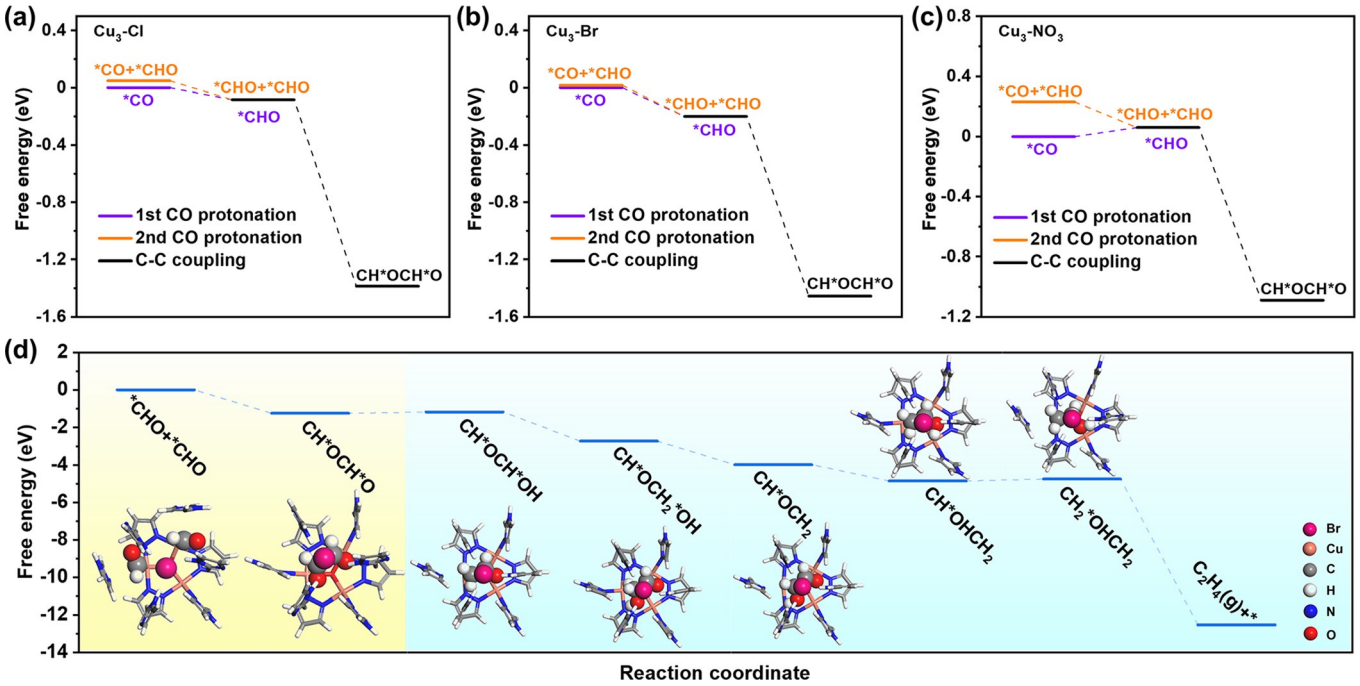

Figure 4. DFT calculations results. The FEDs of CHOCHO pathway taken place on the upside of (a) **Cu_3-Cl**, (b) **Cu_3-Br** and (c) **Cu_3-NO_3**. The violet and orange stepwise lines indicate the paths for the formation of the first and second *CHO from *CO, respectively. The black stepwise lines suggest the C–C coupling through the CHOCHO pathway. (d) Subsequent pathway after the formation of CH*OCH*O on **Cu_3-Br**.

electric field in **Cu_3-X** clusters, which has resulted in the additional stability of the intermediates. Additionally, the steric hindrance of NO_3^- is larger than that of Br^- and Cl^-, so that the surrounding environment of NO_3^- must be deformed when the intermediate is adsorbed. As a result, the *CHO, a more prominent adsorption intermediate than *CO, will cause a larger local rejection and formation enthalpy, which has made the CH*OCH*O formation step an endothermic step for **Cu_3-NO_3**. And correspondingly, **Cu_3-NO_3** gives the worst catalytic performance among the three catalysts. As for Br^- and Cl^-, due to their smaller volume, the adsorption disturbance is much weaker than that of NO_3^-, so that the volumes of *CO and *CHO do not play a decisive role as that in **Cu_3-NO_3**. Besides, since the spatial configurations of *CO and *CHO adsorbed on **Cu_3-Cl** and **Cu_3-Br** are very close (Figure S31), it is considered that Cl^- and Br^- ions only give perturbation effects on adsorption of intermediates. The catalytic performance difference between the **Cu_3-Cl** and **Cu_3-Br** could be explained by the scaling relation between adsorbates.[16] According to the scaling relation, the influence of the surrounding environment on the bond energy change of the adsorption double bond (=CO) is almost twice larger than that of the adsorption single bond (-CHO). Moreover, the energy effects caused by Br^- and Cl^- for the *CHO and *CO adsorption are both rejections. Thus, the rejection to *CO should be stronger than that to *CHO, making the protonation of *CO an exothermic process on both **Cu_3-Br** and **Cu_3-Cl**. Importantly, the rejection to *CHO and *CO caused by Br^- is slightly stronger than that of the Cl^- so that the protonation of *CO and the formation of the *CHO step is more exothermic on **Cu_3-Br**, which has brought the **Cu_3-Br** a better electrocatalytic performance than **Cu_3-Cl**.

Finally, the FEDs of the electrocatalytic reaction pathway after the C–C coupling has been calculated by using the simplified model of the best-performing **Cu_3-Br** catalyst as example. The dominant intermediates and energies involved in each elementary step are summarized in Figure 4d. After the C–C coupling, the H^+/e^- hydrogenation occurred alternatively on O and C of CHO to form CHOH, CH_2OH, and CH_2, respectively. The CH*OCH*O intermediate is then further stepwise reduced to CH*OCH*OH, CH*OCH_2*OH, CH*OCH_2, CH*$OHCH_2$, CH_2*$OHCH_2$ with a corresponding free energy change of 0.07, −1.54, −1.26, −0.87, 0.1 and −7.78 eV.

Conclusion

Based on the structural symmetry of C_2H_4 molecule, three oxygen centered trinuclear copper clusters (**Cu_3-X**) have been designed and synthesized, which feature the symmetrical molecular structure and the appropriate spatial distance between the adjacent catalytically active sites. When the **Cu_3-X** are used as catalysts in electrocatalytic CO_2RR, the selective control of the electrochemical conversion of CO_2 to C_2H_4 has been successfully realized by simply replacing the counter anions in the crystal structure. The DFT calculation results illustrate that the structural characteristics of **Cu_3-X** are beneficial to the simultaneous activation of CO_2 molecules and the C–C coupling between the active intermediates, and finally facilitate the formation of symmetrical C_2H_4 molecule. Among the three catalysts, **Cu_3-Br** exhibits a superior $FE_{C_2H_4}$ of 55.01% with a large current density (129.58 mA cm^{-2}) at −0.7 V (vs. RHE) and could achieve

a long-term catalytic durability. This work provides an important molecular model catalyst system that points out the essential structural characteristics of the catalysts which are suitable for electrochemical conversion of CO_2 to C_2H_4, and more insights for the future design of electrocatalysts which could be applied to efficient reduction of CO_2 to other molecular symmetrical C_{2+} products.

Acknowledgements

This work was financially supported by NSFC (No. 21871141, 21871142, 22071109 and 92061101); the Project funded by China Postdoctoral Science Foundation (No. 2018M630572); the Excellent Youth Foundation of NSF of Jiangsu Province (NO. BK20211593); the Priority Academic Program Development of Jiangsu Higher Education Institutions and the Foundation of Jiangsu Collaborative Innovation Center of Biomedical Functional Materials.

Conflict of Interest

The authors declare no conflict of interest.

Keywords: active sites · C—C coupling · CO_2 reduction · electrocatalysis · molecular catalysts

[1] a) Y. Y. Birdja, E. Pérez-Gallent, M. C. Figueiredo, A. J. Göttle, F. Calle-Vallejo, M. T. M. Koper, *Nat. Energy* **2019**, *4*, 732 – 745; b) C. Tang, Y. Zheng, M. Jaroniec, S.-Z. Qiao, *Angew. Chem. Int. Ed.* **2021**, *60*, 19572 – 19590; *Angew. Chem.* **2021**, *133*, 19724 – 19742; c) K. Zickfeld, D. Azevedo, S. Mathesius, H. D. Matthews, *Nat. Clim. Change* **2021**, *11*, 613 – 617.

[2] a) H. Mistry, A. S. Varela, C. S. Bonifacio, I. Zegkinoglou, I. Sinev, Y.-W. Choi, K. Kisslinger, E. A. Stach, J. C. Yang, P. Strasser, B. R. Cuenya, *Nat. Commun.* **2016**, *7*, 12123; b) C.-T. Dinh, T. Burdyny, M. G. Kibria, A. Seifitokaldani, C. M. Gabardo, F. P. García de Arquer, A. Kiani, J. P. Edwards, P. De Luna, O. S. Bushuyev, C. Zou, R. Quintero-Bermudez, Y. Pang, D. Sinton, E. H. Sargent, *Science* **2018**, *360*, 783; c) J.-Y. Kim, D. Hong, J.-C. Lee, H. G. Kim, S. Lee, S. Shin, B. Kim, H. Lee, M. Kim, J. Oh, G.-D. Lee, D.-H. Nam, Y.-C. Joo, *Nat. Commun.* **2021**, *12*, 3765.

[3] a) D.-H. Nam, O. S. Bushuyev, J. Li, P. De Luna, A. Seifitokaldani, C.-T. Dinh, F. P. García de Arquer, Y. Wang, Z. Liang, A. H. Proppe, C. S. Tan, P. Todorović, O. Shekhah, C. M. Gabardo, J. W. Jo, J. Choi, M.-J. Choi, S.-W. Baek, J. Kim, D. Sinton, S. O. Kelley, M. Eddaoudi, E. H. Sargent, *J. Am. Chem. Soc.* **2018**, *140*, 11378 – 11386; b) P. Shao, W. Zhou, Q.-L. Hong, L. Yi, L. Zheng, W. Wang, H.-X. Zhang, H. Zhang, J. Zhang, *Angew. Chem. Int. Ed.* **2021**, *60*, 16687 – 16692; *Angew. Chem.* **2021**, *133*, 16823 – 16828; c) R. Wang, J. Liu, Q. Huang, L.-Z. Dong, S.-L. Li, Y.-Q. Lan, *Angew. Chem. Int. Ed.* **2021**, *60*, 19829 – 19835; *Angew. Chem.* **2021**, *133*, 19982 – 19988; d) X.-F. Qiu, H.-L. Zhu, J.-R. Huang, P.-Q. Liao, X.-M. Chen, *J. Am. Chem. Soc.* **2021**, *143*, 7242 – 7246.

[4] a) Y. Hori, A. Murata, R. Takahashi, *J. Chem. Soc. Faraday Trans. 1* **1989**, *85*, 2309 – 2326; b) K. Jiang, R. B. Sandberg, A. J. Akey, X. Liu, D. C. Bell, J. K. Nørskov, K. Chan, H. Wang, *Nat. Catal.* **2018**, *1*, 111 – 119; c) D. Gao, R. M. Arán-Ais, H. S. Jeon, B. Roldan Cuenya, *Nat. Catal.* **2019**, *2*, 198 – 210; d) Y. Wang, J. Liu, G. Zheng, *Adv. Mater.* **2021**, https://doi.org/10.1002/adma.202005798; e) X. Yuan, S. Chen, D. Cheng, L. Li, W. Zhu, D. Zhong, Z.-J. Zhao, J. Li, T. Wang, J. Gong, *Angew. Chem. Int. Ed.* **2021**, *60*, 15344 – 15347; *Angew. Chem.* **2021**, *133*, 15472 – 15475.

[5] a) G. L. De Gregorio, T. Burdyny, A. Loiudice, P. Iyengar, W. A. Smith, R. Buonsanti, *ACS Catal.* **2020**, *10*, 4854 – 4862; b) Y. Wang, Z. Wang, C.-T. Dinh, J. Li, A. Ozden, M. Golam Kibria, A. Seifitokaldani, C.-S. Tan, C. M. Gabardo, M. Luo, H. Zhou, F. Li, Y. Lum, C. McCallum, Y. Xu, M. Liu, A. Proppe, A. Johnston, P. Todorovic, T.-T. Zhuang, D. Sinton, S. O. Kelley, E. H. Sargent, *Nat. Catal.* **2020**, *3*, 98 – 106.

[6] a) S. Ma, M. Sadakiyo, M. Heima, R. Luo, R. T. Haasch, J. I. Gold, M. Yamauchi, P. J. A. Kenis, *J. Am. Chem. Soc.* **2017**, *139*, 47 – 50; b) C. G. Morales-Guio, E. R. Cave, S. A. Nitopi, J. T. Feaster, L. Wang, K. P. Kuhl, A. Jackson, N. C. Johnson, D. N. Abram, T. Hatsukade, C. Hahn, T. F. Jaramillo, *Nat. Catal.* **2018**, *1*, 764 – 771; c) J. Huang, M. Mensi, E. Oveisi, V. Mantella, R. Buonsanti, *J. Am. Chem. Soc.* **2019**, *141*, 2490 – 2499; d) I. Merino-Garcia, J. Albo, J. Solla-Gullón, V. Montiel, A. Irabien, *J. CO2 Util.* **2019**, *31*, 135 – 142; e) L. Xiong, X. Zhang, H. Yuan, J. Wang, X. Yuan, Y. Lian, H. Jin, H. Sun, Z. Deng, D. Wang, J. Hu, H. Hu, J. Choi, J. Li, Y. Chen, J. Zhong, J. Guo, M. H. Rümmerli, L. Xu, Y. Peng, *Angew. Chem. Int. Ed.* **2021**, *60*, 2508 – 2518; *Angew. Chem.* **2021**, *133*, 2538 – 2548.

[7] a) C. Chen, X. Sun, L. Lu, D. Yang, J. Ma, Q. Zhu, Q. Qian, B. Han, *Green Chem.* **2018**, *20*, 4579 – 4583; b) Y. Zhou, F. Che, M. Liu, C. Zou, Z. Liang, P. De Luna, H. Yuan, J. Li, Z. Wang, H. Xie, H. Li, P. Chen, E. Bladt, R. Quintero-Bermudez, T.-K. Sham, S. Bals, J. Hofkens, D. Sinton, G. Chen, E. H. Sargent, *Nat. Chem.* **2018**, *10*, 974 – 980; c) W. Ma, S. Xie, T. Liu, Q. Fan, J. Ye, F. Sun, Z. Jiang, Q. Zhang, J. Cheng, Y. Wang, *Nat. Catal.* **2020**, *3*, 478 – 487.

[8] a) K. D. Yang, W. R. Ko, J. H. Lee, S. J. Kim, H. Lee, M. H. Lee, K. T. Nam, *Angew. Chem. Int. Ed.* **2017**, *56*, 796 – 800; *Angew. Chem.* **2017**, *129*, 814 – 818; b) R. M. Arán-Ais, F. Scholten, S. Kunze, R. Rizo, B. Roldan Cuenya, *Nat. Energy* **2020**, *5*, 317 – 325; c) P.-P. Yang, X.-L. Zhang, F.-Y. Gao, Y.-R. Zheng, Z.-Z. Niu, X. Yu, R. Liu, Z.-Z. Wu, S. Qin, L.-P. Chi, Y. Duan, T. Ma, X.-S. Zheng, J.-F. Zhu, H.-J. Wang, M.-R. Gao, S.-H. Yu, *J. Am. Chem. Soc.* **2020**, *142*, 6400 – 6408.

[9] a) Y.-R. Wang, Q. Huang, C.-T. He, Y. Chen, J. Liu, F.-C. Shen, Y.-Q. Lan, *Nat. Commun.* **2018**, *9*, 4466; b) Q. Huang, Q. Li, J. Liu, Y. R. Wang, R. Wang, L. Z. Dong, Y. H. Xia, J. L. Wang, Y.-Q. Lan, *Matter* **2019**, *1*, 1656 – 1668; c) N. Li, J. Liu, B.-X. Dong, Y.-Q. Lan, *Angew. Chem. Int. Ed.* **2020**, *59*, 20779 – 20793; *Angew. Chem.* **2020**, *132*, 20963 – 20977; d) M. Lu, M. Zhang, C.-G. Liu, J. Liu, L.-J. Shang, M. Wang, J.-N. Chang, S.-L. Li, Y.-Q. Lan, *Angew. Chem. Int. Ed.* **2021**, *60*, 4864 – 4871; *Angew. Chem.* **2021**, *133*, 4914 – 4921; e) S.-N. Sun, N. Li, J. Liu, W.-X. Ji, L.-Z. Dong, Y.-R. Wang, Y.-Q. Lan, *Natl. Sci. Rev.* **2021**, *8*, nwaa195; f) L. Zhang, X.-X. Li, Z.-L. Lang, Y. Liu, J. Liu, L. Yuan, W.-Y. Lu, Y.-S. Xia, L.-Z. Dong, D.-Q. Yuan, Y.-Q. Lan, *J. Am. Chem. Soc.* **2021**, *143*, 3808 – 3816.

[10] a) J.-P. Zhang, Y.-B. Zhang, J.-B. Lin, X.-M. Chen, *Chem. Rev.* **2012**, *112*, 1001 – 1033; b) K. Wang, X.-L. Lv, D. Feng, J. Li, S. Chen, J. Sun, L. Song, Y. Xie, J.-R. Li, H.-C. Zhou, *J. Am. Chem. Soc.* **2016**, *138*, 914 – 919.

[11] F. Lei, W. Liu, Y. Sun, J. Xu, K. Liu, L. Liang, T. Yao, B. Pan, S. Wei, Y. Xie, *Nat. Commun.* **2016**, *7*, 12697.

[12] I. Merino-Garcia, J. Albo, A. Irabien, *Nanotechnology* **2018**, *29*, 014001.

[13] C. V. Niveditha, M. J. J. Fatima, S. Sindhu, *J. Electrochem. Soc.* **2016**, *163*, H426 – H433.

[14] a) Z. Weng, J. Jiang, Y. Wu, Z. Wu, X. Guo, K. L. Materna, W. Liu, V. S. Batista, G. W. Brudvig, H. Wang, *J. Am. Chem. Soc.* **2016**, *138*, 8076 – 8079; b) S. Kusama, T. Saito, H. Hashiba, A. Sakai, S. Yotsuhashi, *ACS Catal.* **2017**, *7*, 8382 – 8385; c) Y.-L.

Qiu, H.-X. Zhong, T.-T. Zhang, W.-B. Xu, P.-P. Su, X.-F. Li, H.-M. Zhang, *ACS Appl. Mater. Interfaces* **2018**, *10*, 2480 – 2489; d) Y. Zhou, S. Chen, S. Xi, Z. Wang, P. Deng, F. Yang, Y. Han, Y. Pang, B. Y. Xia, *Cell Rep. Phys. Sci.* **2020**, *1*, 100182.

[15] S. Nitopi, E. Bertheussen, S. B. Scott, X. Liu, A. K. Engstfeld, S. Horch, B. Seger, I. E. L. Stephens, K. Chan, C. Hahn, J. K. Nørskov, T. F. Jaramillo, I. Chorkendorff, *Chem. Rev.* **2019**, *119*, 7610 – 7672.

[16] F. Abild-Pedersen, J. Greeley, F. Studt, J. Rossmeisl, T. R. Munter, P. G. Moses, E. Skúlason, T. Bligaard, J. K. Nørskov, *Phys. Rev. Lett.* **2007**, *99*, 016105.

Manuscript received: August 20, 2021
Accepted manuscript online: September 29, 2021
Version of record online: November 9, 2021

